
This is an electronic reprint of the original article.
This reprint *may differ* from the original in pagination and typographic detail.

Author(s): Adare, A.; Afanasiev, S.; Aidala, C.; Ajitanand, N. N.; Akiba, Y.; Al-Bataineh, H.; Alexander, J.; Angerami, A.; Aoki, K.; Apadula, N.; Kim, Dong Jo; Rak, Jan

Title: Measurement of transverse-single-spin asymmetries for midrapidity and forward-rapidity production of hadrons in polarized p plus p collisions at $\sqrt{s}=200$ and 62.4 GeV

Year: 2014

Version:

Please cite the original version:

Adare, A., Afanasiev, S., Aidala, C., Ajitanand, N.N., Akiba, Y., Al-Bataineh, H., Alexander, J., Angerami, A., Aoki, K., Apadula, N., Kim, D. J., & Rak, J. (2014). Measurement of transverse-single-spin asymmetries for midrapidity and forward-rapidity production of hadrons in polarized p plus p collisions at $\sqrt{s}=200$ and 62.4 GeV. *Physical Review D*, 90(1), Article 01200. <https://doi.org/10.1103/PhysRevD.90.012006>

All material supplied via JYX is protected by copyright and other intellectual property rights, and duplication or sale of all or part of any of the repository collections is not permitted, except that material may be duplicated by you for your research use or educational purposes in electronic or print form. You must obtain permission for any other use. Electronic or print copies may not be offered, whether for sale or otherwise to anyone who is not an authorised user.

Measurement of transverse-single-spin asymmetries for midrapidity and forward-rapidity production of hadrons in polarized $p + p$ collisions at $\sqrt{s} = 200$ and 62.4 GeV

A. Adare,¹⁴ S. Afanasiev,³¹ C. Aidala,^{44,45} N. N. Ajitanand,⁶³ Y. Akiba,^{57,58} H. Al-Bataineh,⁵¹ J. Alexander,⁶³ A. Angerami,¹⁵ K. Aoki,^{36,57} N. Apadula,⁶⁴ L. Aphecetche,⁶⁵ Y. Aramaki,^{13,57} J. Asai,⁵⁷ E. T. Atomssa,³⁷ R. Averbeck,⁶⁴ T. C. Awes,⁵³ B. Azmoun,⁸ V. Babintsev,²⁵ M. Bai,⁷ G. Baksay,²¹ L. Baksay,²¹ A. Baldissieri,¹⁷ K. N. Barish,⁹ P. D. Barnes,^{40,*} B. Bassalleck,⁵⁰ A. T. Basye,¹ S. Bathe,^{6,9,58} S. Batsouli,⁵³ V. Baublis,⁵⁶ C. Baumann,⁴⁶ A. Bazilevsky,⁸ S. Belikov,^{8,*} R. Belmont,⁶⁹ R. Bennett,⁶⁴ A. Berdnikov,⁶⁰ Y. Berdnikov,⁶⁰ J. H. Bhom,⁷³ A. A. Bickley,¹⁴ D. S. Blau,³⁵ J. G. Boissevain,⁴⁰ J. S. Bok,⁷³ H. Borel,¹⁷ K. Boyle,⁶⁴ M. L. Brooks,⁴⁰ H. Buesching,⁸ V. Bumazhnov,²⁵ G. Bunce,^{8,58} S. Butsyk,⁴⁰ C. M. Camacho,⁴⁰ S. Campbell,⁶⁴ A. Carinci,⁴⁷ B. S. Chang,⁷³ W. C. Chang,² J.-L. Charvet,¹⁷ C.-H. Chen,⁶⁴ S. Chernichenko,²⁵ C. Y. Chi,¹⁵ M. Chiu,^{8,26} I. J. Choi,⁷³ J. B. Choi,¹¹ R. K. Choudhury,⁵ P. Christiansen,⁴² T. Chujo,⁶⁸ P. Chung,⁶³ A. Churny,²⁵ O. Chvala,⁹ V. Cianciolo,⁵³ Z. Citron,⁶⁴ B. A. Cole,¹⁵ Z. Conesa del Valle,³⁷ M. Connors,⁶⁴ P. Constantin,⁴⁰ M. Csanád,¹⁹ T. Csörgő,⁷² T. Dahms,⁶⁴ S. Dairaku,⁶⁹ I. Danchev,⁶⁹ K. Das,²² A. Datta,⁴⁴ G. David,⁸ M. K. Dayananda,²³ A. Denisov,²⁵ D. d'Enterria,³⁷ A. Deshpande,^{58,64} E. J. Desmond,⁸ K. V. Dharmawardane,⁵¹ O. Dietzsch,⁶¹ A. Dion,^{29,64} M. Donadelli,⁶¹ O. Drapier,³⁷ A. Drees,⁶⁴ K. A. Drees,⁷ A. K. Dubey,⁷¹ J. M. Durham,^{40,64} A. Durum,²⁵ D. Dutta,⁵ V. Dzhordzhadze,⁹ L. D'Orazio,⁴³ S. Edwards,²² Y. V. Efremenko,⁵³ F. Ellinghaus,¹⁴ T. Engelmere,¹⁵ A. Enokizono,^{39,53} H. En'yo,^{57,58} S. Esumi,⁶⁸ K. O. Eyser,⁹ B. Fadern,⁴⁷ N. Feege,⁶⁴ D. E. Fields,^{50,58} M. Finger,¹⁰ M. Finger, Jr.,¹⁰ F. Fleuret,³⁷ S. L. Fokin,³⁵ Z. Fraenkel,^{71,*} J. E. Frantz,^{52,64} A. Franz,⁸ A. D. Frawley,²² K. Fujiwara,⁵⁷ Y. Fukao,^{36,57} T. Fusayasu,⁴⁹ I. Garishvili,⁶⁶ A. Glenn,^{14,39} H. Gong,⁶⁴ M. Gonin,³⁷ J. Gosset,¹⁷ Y. Goto,^{57,58} R. Granier de Cassagnac,³⁷ N. Grau,^{3,15} S. V. Greene,⁶⁹ G. Grim,⁴⁰ M. Grosse Perdekamp,^{26,58} T. Gunji,¹³ H.-Å. Gustafsson,^{42,*} A. Hadj Henni,⁶⁵ J. S. Haggerty,⁸ K. I. Hahn,²⁰ H. Hamagaki,¹³ J. Hamblen,⁶⁶ R. Han,⁵⁵ J. Hanks,¹⁵ E. P. Hartouni,³⁹ K. Haruna,²⁴ E. Haslum,⁴² R. Hayano,¹³ X. He,²³ M. Heffner,³⁹ T. K. Hemmick,⁶⁴ T. Hester,¹⁷ J. C. Hill,²⁹ M. Hohmann,²¹ W. Holzmann,^{15,63} K. Homma,²⁴ B. Hong,³⁴ T. Horaguchi,^{13,24,57,67} D. Hornback,⁶⁶ S. Huang,⁶⁹ T. Ichihara,^{57,58} R. Ichimiya,⁵⁷ H. Iinuma,^{36,57} Y. Ikeda,⁶⁸ K. Imai,^{30,36,57} J. Imrek,¹⁸ M. Inaba,⁶⁸ D. Isenhowe,¹ M. Ishihara,⁵⁷ T. Isobe,^{13,57} M. Issah,^{63,69} A. Isupov,³¹ D. Ivanishev,⁵⁶ Y. Iwanaga,²⁴ B. V. Jacak,⁶⁴ J. Jia,^{8,15,63} X. Jiang,⁴⁰ J. Jin,¹⁵ B. M. Johnson,⁸ T. Jones,¹ K. S. Joo,⁴⁸ D. Jouan,⁵⁴ D. S. Jumper,¹ F. Kajihara,¹³ S. Kametani,⁵⁷ N. Kamihara,⁵⁸ J. Kamin,⁶⁴ J. H. Kang,⁷³ J. Kapustinsky,⁴⁰ K. Karatsu,^{36,57} M. Kasai,^{57,59} D. Kaway,^{44,58} M. Kawashima,^{57,59} A. V. Kazantsev,³⁵ T. Kempel,²⁹ A. Khanzadeev,⁵⁶ K. M. Kijima,²⁴ J. Kikuchi,⁷⁰ A. Kim,²⁰ B. I. Kim,³⁴ D. H. Kim,⁴⁸ D. J. Kim,^{32,73} E. Kim,⁶² E.-J. Kim,¹¹ S. H. Kim,⁷³ Y.-J. Kim,²⁶ E. Kinney,¹⁴ K. Kiriluk,¹⁴ Á. Kiss,¹⁹ E. Kistenev,⁸ J. Klay,³⁹ C. Klein-Boesing,⁴⁶ D. Kleinjan,⁹ L. Kochenda,⁵⁶ B. Komkov,⁵⁶ M. Konno,⁶⁸ J. Koster,²⁶ A. Kozlov,⁷¹ A. Král,¹⁶ A. Kravitz,¹⁵ G. J. Kunde,⁴⁰ K. Kurita,^{57,59} M. Kurosawa,⁵⁷ M. J. Kweon,³⁴ Y. Kwon,^{66,73} G. S. Kyle,⁵¹ R. Lacey,⁶³ Y. S. Lai,¹⁵ J. G. Lajoie,²⁹ D. Layton,²⁶ A. Lebedev,²⁹ D. M. Lee,⁴⁰ J. Lee,²⁰ K. B. Lee,³⁴ K. S. Lee,³⁴ T. Lee,⁶² M. J. Leitch,⁴⁰ M. A. L. Leite,⁶¹ B. Lenzi,⁶¹ X. Li,¹² P. Lichtenwalner,⁴⁷ P. Liebing,⁵⁸ L. A. Linden Levy,¹⁴ T. Liška,¹⁶ A. Litvinenko,³¹ H. Liu,^{40,51} M. X. Liu,⁴⁰ B. Love,⁶⁹ D. Lynch,⁸ C. F. Maguire,⁶⁹ Y. I. Makdisi,⁷ A. Malakhov,³¹ M. D. Malik,⁵⁰ V. I. Manko,³⁵ E. Mannel,¹⁵ Y. Mao,^{55,57} L. Mašek,^{10,28} H. Masui,⁶⁸ F. Matathias,¹⁵ M. McCumber,⁶⁴ P. L. McGaughey,⁴⁰ D. McGlinchey,^{14,22} N. Means,⁶⁴ B. Meredith,²⁶ Y. Miake,⁶⁸ T. Mibe,³³ A. C. Mignerey,⁴³ P. Mikeš,²⁸ K. Miki,^{57,68} A. Milov,⁸ M. Mishra,⁴ J. T. Mitchell,⁸ A. K. Mohanty,⁵ H. J. Moon,⁴⁸ Y. Morino,¹³ A. Morreale,⁹ D. P. Morrison,^{8,†} T. V. Moukhanova,³⁵ D. Mukhopadhyay,⁶⁹ T. Murakami,³⁶ J. Murata,^{57,59} S. Nagamiya,³³ J. L. Nagle,^{14,‡} M. Naglis,⁷¹ M. I. Nagy,^{19,72} I. Nakagawa,^{57,58} Y. Nakamiya,²⁴ K. R. Nakamura,^{36,57} T. Nakamura,^{24,57} K. Nakano,^{57,67} S. Nam,²⁰ J. Newby,³⁹ M. Nguyen,⁶⁴ M. Nishashi,²⁴ T. Niida,⁶⁸ R. Nouicer,⁸ A. S. Nyanin,³⁵ C. Oakley,²³ E. O'Brien,⁸ S. X. Oda,¹³ C. A. Ogilvie,²⁹ M. Oka,⁶⁸ K. Okada,⁵⁸ Y. Onuki,⁵⁷ A. Oskarsson,⁴² M. Ouchida,^{24,57} K. Ozawa,¹³ R. Pak,⁸ A. P. T. Palounek,⁴⁰ V. Pantuev,^{27,64} V. Papavassiliou,⁵¹ I. H. Park,²⁰ J. Park,⁶² S. K. Park,³⁴ W. J. Park,³⁴ S. F. Pate,⁵¹ H. Pei,²⁹ J.-C. Peng,²⁶ H. Pereira,¹⁷ V. Peresedov,³¹ D. Yu. Peressounko,³⁵ R. Petti,⁶⁴ C. Pinkenburg,⁷¹ R. P. Pisani,⁸ M. Proissl,⁶⁴ M. L. Purschke,⁸ A. K. Purwar,⁴⁰ H. Qu,²³ J. Rak,^{32,50} A. Rakotozafindrabe,³⁷ I. Ravinovich,⁷¹ K. F. Read,^{53,66} S. Rembeczki,²¹ K. Reygers,⁴⁶ V. Riabov,⁵⁶ Y. Riabov,⁵⁶ E. Richardson,⁴³ D. Roach,⁶⁹ G. Roche,⁴¹ S. D. Rolnick,⁹ M. Rosati,²⁹ C. A. Rosen,¹⁴ S. S. E. Rosendahl,⁴² P. Rosnet,⁴¹ P. Rukoyatkin,³¹ P. Ružička,³¹ V. L. Rykov,⁵⁷ B. Sahlmueller,^{46,64} N. Saito,^{33,36,57,58} T. Sakaguchi,^{57,67} S. Sakai,⁶⁸ K. Sakashita,^{57,67} V. Samsonov,⁵⁶ S. Sano,^{13,70} T. Sato,⁶⁸ S. Sawada,³³ K. Sedgwick,⁹ J. Seele,¹⁴ R. Seidl,^{26,58} A. Yu. Semenov,²⁹ V. Semenov,^{25,27} R. Seto,⁹ D. Sharma,⁷¹ I. Shein,²⁵ T.-A. Shibata,^{57,67} K. Shigaki,²⁴ M. Shimomura,⁶⁸ K. Shoji,^{36,57} P. Shukla,⁵ A. Sickles,⁸ C. L. Silva,^{29,61} D. Silvermyr,⁵³ C. Silvestre,¹⁷ K. S. Sim,³⁴ B. K. Singh,⁴ C. P. Singh,⁴ V. Singh,⁴ M. Slunečka,¹⁰ A. Soldatov,²⁵ R. A. Soltz,³⁹ W. E. Sondheim,⁴⁰ S. P. Sorensen,⁶⁶ I. V. Sourikova,⁸ F. Staley,¹⁷ P. W. Stankus,⁵³ E. Stenlund,⁴² M. Stepanov,⁵¹ A. Ster,⁷² S. P. Stoll,⁸ T. Sugitate,²⁴ C. Suire,⁵⁴ A. Sukhanov,⁸ J. Sziklai,⁷² E. M. Takagui,⁶¹ A. Taketani,^{57,58} R. Tanabe,⁶⁸ Y. Tanaka,⁴⁹ S. Taneja,⁶⁴ K. Tanida,^{36,57,58,62} M. J. Tannenbaum,⁸ S. Tarafdar,⁴ A. Taranenko,⁶³ P. Tarján,¹⁸ H. Themann,⁶⁴ D. Thomas,¹ T. L. Thomas,⁵⁰ M. Togawa,^{36,57,58} A. Toia,⁶⁴ L. Tomášek,²⁸ Y. Tomita,⁶⁸ H. Torii,^{24,57} R. S. Towell,¹ V.-N. Tram,³⁷

I. Tserruya,⁷¹ Y. Tsuchimoto,²⁴ C. Vale,^{8,29} H. Valle,⁶⁹ H. W. van Hecke,⁴⁰ E. Vazquez-Zambrano,¹⁵ A. Veicht,²⁶ J. Velkovska,⁶⁹ R. Vértési,^{18,72} A. A. Vinogradov,³⁵ M. Virius,¹⁶ A. Vossen,²⁶ V. Vrba,²⁸ E. Vznuzdaev,⁵⁶ X. R. Wang,⁵¹ D. Watanabe,²⁴ K. Watanabe,⁶⁸ Y. Watanabe,^{57,58} F. Wei,²⁹ R. Wei,⁶³ J. Wessels,⁴⁶ S. N. White,⁸ D. Winter,¹⁵ C. L. Woody,⁸ R. M. Wright,¹ M. Wysocki,¹⁴ W. Xie,⁵⁸ Y. L. Yamaguchi,^{13,57,70} K. Yamaura,²⁴ R. Yang,²⁶ A. Yanovich,²⁵ J. Ying,²³ S. Yokkaichi,^{57,58} Z. You,⁵⁵ G. R. Young,⁵³ I. Younus,^{38,50} I. E. Yushmanov,³⁵ W. A. Zajc,¹⁵ O. Zaudtke,⁴⁶ C. Zhang,⁵³ S. Zhou,¹² and L. Zolin³¹

(PHENIX Collaboration)

¹Abilene Christian University, Abilene, Texas 79699, USA

²Institute of Physics, Academia Sinica, Taipei 11529, Taiwan

³Department of Physics, Augustana College, Sioux Falls, South Dakota 57197, USA

⁴Department of Physics, Banaras Hindu University, Varanasi 221005, India

⁵Bhabha Atomic Research Centre, Bombay 400 085, India

⁶Baruch College, City University of New York, New York, New York, 10010 USA

⁷Collider-Accelerator Department, Brookhaven National Laboratory, Upton, New York 11973-5000, USA

⁸Physics Department, Brookhaven National Laboratory, Upton, New York 11973-5000, USA

⁹University of California - Riverside, Riverside, California 92521, USA

¹⁰Charles University, Ovocný trh 5, Praha 1, 116 36 Prague, Czech Republic

¹¹Chonbuk National University, Jeonju, 561-756, Korea

¹²Science and Technology on Nuclear Data Laboratory, China Institute of Atomic Energy, Beijing 102413, People's Republic of China

¹³Center for Nuclear Study, Graduate School of Science, University of Tokyo, 7-3-1 Hongo, Bunkyo, Tokyo 113-0033, Japan

¹⁴University of Colorado, Boulder, Colorado 80309, USA

¹⁵Columbia University, New York, New York 10027 and Nevis Laboratories, Irvington, New York 10533, USA

¹⁶Czech Technical University, Zikova 4, 166 36 Prague 6, Czech Republic

¹⁷Dapnia, CEA Saclay, F-91191 Gif-sur-Yvette, France

¹⁸Debrecen University, H-4010 Debrecen, Egyetem tr 1, Hungary

¹⁹ELTE, Eötvös Loránd University, H-1117 Budapest, Pázmány Péter sétány 1/A, Hungary

²⁰Ewha Womans University, Seoul 120-750, Korea

²¹Florida Institute of Technology, Melbourne, Florida 32901, USA

²²Florida State University, Tallahassee, Florida 32306, USA

²³Georgia State University, Atlanta, Georgia 30303, USA

²⁴Hiroshima University, Kagamiyama, Higashi-Hiroshima 739-8526, Japan

²⁵IHEP Protvino, State Research Center of Russian Federation, Institute for High Energy Physics, Protvino 142281, Russia

²⁶University of Illinois at Urbana-Champaign, Urbana, Illinois 61801, USA

²⁷Institute for Nuclear Research of the Russian Academy of Sciences, prospekt 60-letiya Oktyabrya 7a, Moscow 117312, Russia

²⁸Institute of Physics, Academy of Sciences of the Czech Republic, Na Slovance 2, 182 21 Prague 8, Czech Republic

²⁹Iowa State University, Ames, Iowa 50011, USA

³⁰Advanced Science Research Center, Japan Atomic Energy Agency, 2-4 Shirakata Shirane, Tokai-mura, Naka-gun, Ibaraki-ken 319-1195, Japan

³¹Joint Institute for Nuclear Research, 141980 Dubna, Moscow Region, Russia

³²Helsinki Institute of Physics and University of Jyväskylä, P.O. Box 35, FI-40014 Jyväskylä, Finland

³³KEK, High Energy Accelerator Research Organization, Tsukuba, Ibaraki 305-0801, Japan

³⁴Korea University, Seoul 136-701, Korea

³⁵Russian Research Center "Kurchatov Institute," Moscow 123098, Russia

³⁶Kyoto University, Kyoto 606-8502, Japan

³⁷Laboratoire Leprince-Ringuet, Ecole Polytechnique, CNRS-IN2P3, Route de Saclay, F-91128 Palaiseau, France

³⁸Physics Department, Lahore University of Management Sciences, Lahore 54792, Pakistan

³⁹Lawrence Livermore National Laboratory, Livermore, California 94550, USA

⁴⁰Los Alamos National Laboratory, Los Alamos, New Mexico 87545, USA

⁴¹LPC, Université Blaise Pascal, CNRS-IN2P3, Clermont-Fd, 63177 Aubiere Cedex, France

⁴²Department of Physics, Lund University, Box 118, SE-221 00 Lund, Sweden

- ⁴³University of Maryland, College Park, Maryland 20742, USA
- ⁴⁴Department of Physics, University of Massachusetts, Amherst, Massachusetts 01003-9337, USA
- ⁴⁵Department of Physics, University of Michigan, Ann Arbor, Michigan 48109-1040, USA
- ⁴⁶Institut für Kernphysik, University of Muenster, D-48149 Muenster, Germany
- ⁴⁷Muhlenberg College, Allentown, Pennsylvania 18104-5586, USA
- ⁴⁸Myongji University, Yongin, Kyonggido 449-728, Korea
- ⁴⁹Nagasaki Institute of Applied Science, Nagasaki-shi, Nagasaki 851-0193, Japan
- ⁵⁰University of New Mexico, Albuquerque, New Mexico 87131, USA
- ⁵¹New Mexico State University, Las Cruces, New Mexico 88003, USA
- ⁵²Department of Physics and Astronomy, Ohio University, Athens, Ohio 45701, USA
- ⁵³Oak Ridge National Laboratory, Oak Ridge, Tennessee 37831, USA
- ⁵⁴IPN-Orsay, Université Paris Sud, CNRS-IN2P3, BP1, F-91406 Orsay, France
- ⁵⁵Peking University, Beijing 100871, People's Republic of China
- ⁵⁶PNPI, Petersburg Nuclear Physics Institute, Gatchina, Leningrad region 188300, Russia
- ⁵⁷RIKEN Nishina Center for Accelerator-Based Science, Wako, Saitama 351-0198, Japan
- ⁵⁸RIKEN BNL Research Center, Brookhaven National Laboratory, Upton, New York 11973-5000, USA
- ⁵⁹Physics Department, Rikkyo University, 3-34-1 Nishi-Ikebukuro, Toshima, Tokyo 171-8501, Japan
- ⁶⁰Saint Petersburg State Polytechnic University, St. Petersburg 195251, Russia
- ⁶¹Universidade de São Paulo, Instituto de Física, Caixa Postal 66318, São Paulo CEP05315-970, Brazil
- ⁶²Department of Physics and Astronomy, Seoul National University, Seoul 151-742, Korea
- ⁶³Chemistry Department, Stony Brook University, SUNY, Stony Brook, New York 11794-3400, USA
- ⁶⁴Department of Physics and Astronomy, Stony Brook University, SUNY, Stony Brook, New York 11794-3400, USA
- ⁶⁵SUBATECH (Ecole des Mines de Nantes, CNRS-IN2P3, Université de Nantes) BP 20722 - 44307, Nantes, France
- ⁶⁶University of Tennessee, Knoxville, Tennessee 37996, USA
- ⁶⁷Department of Physics, Tokyo Institute of Technology, Oh-okayama, Meguro, Tokyo 152-8551, Japan
- ⁶⁸Institute of Physics, University of Tsukuba, Tsukuba, Ibaraki 305, Japan
- ⁶⁹Vanderbilt University, Nashville, Tennessee 37235, USA
- ⁷⁰Waseda University, Advanced Research Institute for Science and Engineering, 17 Kikui-cho, Shinjuku-ku, Tokyo 162-0044, Japan
- ⁷¹Weizmann Institute, Rehovot 76100, Israel
- ⁷²Institute for Particle and Nuclear Physics, Wigner Research Centre for Physics, Hungarian Academy of Sciences (Wigner RCP, RMKI) Budapest 114, H-1525 Budapest, P.O. Box 49, Hungary
- ⁷³Yonsei University, IPAP, Seoul 120-749, Korea
- (Received 8 December 2013; published 17 July 2014)

Measurements of transverse-single-spin asymmetries (A_N) in $p + p$ collisions at $\sqrt{s} = 62.4$ and 200 GeV with the PHENIX detector at the Relativistic Heavy Ion Collider are presented. At midrapidity, A_N is measured for neutral pion and eta mesons reconstructed from diphoton decay, and, at forward rapidities, neutral pions are measured using both diphotons and electromagnetic clusters. The neutral-pion measurement of A_N at midrapidity is consistent with zero with uncertainties a factor of 20 smaller than previous publications, which will lead to improved constraints on the gluon Sivers function. At higher rapidities, where the valence quark distributions are probed, the data exhibit sizable asymmetries. In comparison with previous measurements in this kinematic region, the new data extend the kinematic coverage in \sqrt{s} and p_T , and it is found that the asymmetries depend only weakly on \sqrt{s} . The origin of the forward A_N is presently not understood quantitatively. The extended reach to higher p_T probes the transition between transverse momentum dependent effects at low p_T and multiparton dynamics at high p_T .

DOI: 10.1103/PhysRevD.90.012006

PACS numbers: 13.85.Ni, 13.88.+e, 14.20.Dh, 25.75.Dw

I. INTRODUCTION

The proton is a fundamental and stable bound state of quantum chromodynamics. Collinear perturbative quantum chromodynamics (pQCD) at leading twist in the operator product expansion successfully describes the quark and gluon substructure of the proton observed in high energy scattering experiments [1]. The parton distribution

*Deceased.

†PHENIX Co-Spokesperson.
morrisson@bnl.gov

‡PHENIX Co-Spokesperson.
jamie.nagle@colorado.edu

functions, $f_i(x, Q^2)$, constitute the number densities of partons of flavor i in the proton. They depend on the partonic momentum fraction, x , and on the momentum transfer scale, Q^2 . Two similar sets of distribution functions parametrize the spin dependent parton distributions in protons polarized either longitudinally or transversely with respect to the proton momentum direction [2]. The longitudinally polarized structure has been successfully described using pQCD at leading twist [3].

Initially, transverse-single-spin asymmetries or the analyzing power (A_N) of hadrons h produced in the transversely polarized $p^\uparrow + p \rightarrow h + X$ reaction were expected to be small [4], but experiments instead measured large asymmetries of up to $A_N \approx 40\%$. These asymmetries have been measured at increasing center-of-mass energies \sqrt{s} over the past three decades, from 4.9 to 200 GeV [5–10]. Recent results from the Relativistic Heavy Ion Collider (RHIC) show that large asymmetries persist even up to $\sqrt{s} = 200$ GeV [11–13]. Unlike at the low to intermediate energies, the measured unpolarized cross section at high energies is well reproduced by pQCD calculations [11,13], indicating that unpolarized collisions can be described by the standard collinear factorized theory, while transversely polarized collisions cannot.

To better describe the large A_N measurements, the theoretical framework has been extended to include transverse momentum dependent (TMD) distributions and multiparton dynamics (higher twist effects). Because the intrinsic partonic transverse momentum scale is set by the mass of the proton, these effects dominate for hadrons with low momenta transverse to the beam axis, $p_T \lesssim 1$ GeV/ c . At least two TMD effects have been proposed to explain the observed nonzero asymmetries.

The first of these, known as the Sivers effect, correlates the proton spin with the partonic transverse momentum k_T [14]. It has been measured in semi-inclusive deep inelastic scattering (SIDIS) experiments with sensitivity mainly to the quarks [15,16]. Previous results in $p + p$ collisions [17] have been used to constrain the gluon Sivers function [18]. Recently, this function has received intense theoretical attention based on questions of universality and an expected sign change of A_N in SIDIS compared to Drell-Yan production [19,20].

At large transverse momenta the collinear higher twist effects are thought to become more important in the creation of transverse spin asymmetries [21,22]. For Drell-Yan production it has been shown that both initial state TMD (Sivers) and multiparton dynamics provide equivalent descriptions of transverse asymmetries in an overlap region at intermediate transverse momenta [23]. With increasing p_T the asymmetries are expected to fall off and vanish in the strictly collinear regime, which has not been observed experimentally yet. It is best probed at high center-of-mass energies, where the range of transverse momenta is wider.

A second transverse momentum dependent effect, known as the Collins effect, describes the coupling of a transverse quark polarization (transversity) and a transverse spin dependent fragmentation from a struck quark into a hadron [24]. The full integral over all partonic momenta $0 \leq x \leq 1$ of the transversity distribution can be compared to the flavor-singlet tensor charge $\delta\Sigma$, which is calculable in lattice QCD [25,26]. This will be a fundamental test of the theory.

The spin dependent fragmentation part has been measured in $e^+ + e^-$ annihilation for charged pions [27,28] and serves as input for Collins asymmetries in SIDIS to access the transversity distribution [29–31]. Attempts have been made to use the same Collins fragmentation functions and the transversity distribution derived from SIDIS to describe the asymmetries in polarized proton data [32]. Recently, a collinear higher twist framework has been extended to describe the fragmentation contribution to these asymmetries as well [33].

This paper reports on measurements of A_N at $\sqrt{s} = 62.4$ and 200 GeV. The data were taken by the PHENIX experiment at RHIC in the years 2006 ($\sqrt{s} = 62.4$ GeV) and 2008 ($\sqrt{s} = 200$ GeV) with integrated luminosities of 42 nb $^{-1}$ and 4.3 pb $^{-1}$, respectively. Results are presented for neutral mesons in a midrapidity region ($|\eta| < 0.35$) as well as for π^0 mesons and inclusive electromagnetic clusters at forward/backward pseudorapidities ($3.1 < |\eta| < 3.8$). Section II describes the experimental setup along with the properties of the polarized proton beams. The formalism of transverse-single-spin asymmetries is introduced in Sec. III before details of the analysis procedure are specified. A general discussion of the results and their possible implications for nucleon structure and contributing asymmetry mechanisms concludes this paper in Sec. IV.

II. EXPERIMENTAL SETUP

A. PHENIX midrapidity and global detectors

The PHENIX midrapidity spectrometer is used to detect neutral pions and η mesons via their decay into two photons. The spectrometer covers a pseudorapidity range of $|\eta| < 0.35$ and is split into two approximately back-to-back arms each covering $\Delta\phi = \pi/2$ in azimuth. The electromagnetic calorimeter (EMCal) is highly segmented with $\Delta\eta \times \Delta\phi \approx 0.01 \times 0.01$. Events are selected using an EMCal based high tower energy trigger in coincidence with a minimum bias trigger. The trigger, digitization electronics, and details of the hardware have been discussed previously [34]. The trigger efficiency starts at about 5% for neutral pions with $p_T \approx 1$ GeV/ c and rises to and saturates at about 90% at $p_T > 3.5$ GeV/ c . A multiwire proportional chamber with pad readout [35] is situated in front of the calorimeter face, and is used to veto charged particles.

The minimum bias trigger was defined as the coincidence of signals from two beam beam counters (BBCs) covering the full azimuthal angle and the pseudorapidity range $3.0 < |\eta| < 3.9$ [36]. The BBCs are used to reconstruct the collision time and the collision (vertex) position along the beam direction. Each BBC is situated 144 cm from the nominal interaction point and comprises an array of 64 counters arranged around the beam pipe. Each counter comprises a Čerenkov quartz radiator of hexagonal cross section with a mesh dynode photomultiplier tube for readout.

B. Muon piston calorimeter

The PHENIX muon piston calorimeter (MPC) is an electromagnetic calorimeter which was designed to measure photons and neutral mesons at forward rapidity. The detector comprises two separate devices placed along the beamline to the north and to the south of the nominal interaction point, labeled N-MPC and S-MPC, respectively. The S-MPC was first installed in 2006 and the N-MPC followed a year later. Therefore, the analysis of the 2006 data set ($\sqrt{s} = 62.4$ GeV) uses only the S-MPC while the 2008 data set ($\sqrt{s} = 200$ GeV) includes both detectors.

Both MPCs are located in cavities of the steel piston which is part of the PHENIX muon detector magnet yoke. The diameter of each cavity limits the detector's outer diameter to 45 cm, while the beam pipe requires an inner diameter of no less than 8 cm (N-MPC) or 10 cm (S-MPC). The MPCs are placed ± 220 cm from the nominal interaction point and are composed of 192 (S-MPC) or 220 (N-MPC) towers stacked to form an annulus around the beam pipe. The detector acceptance covers the full azimuthal angle and a pseudorapidity range of $-3.8 < \eta < -3.1$ south and $3.1 < \eta < 3.9$ north of the nominal interaction point.

Each tower combines a PbWO_4 scintillating crystal wrapped with Tyvek, aluminized Mylar and MonoKote, with a Hamamatsu S8664-55 avalanche photodiode for readout. Each crystal measures $2.2 \times 2.2 \times 18 \text{ cm}^3$, corresponding to a depth of 21.2 radiation lengths and 0.844 nuclear interaction lengths. Independently of the minimum bias trigger, the MPC is equipped with its own high energy cluster trigger. The trigger and digitization electronics are identical to those of the EMCal and are discussed in detail in [34]. For the presented data, the trigger efficiency starts at 5% for photon energies $E \approx 30$ GeV and reaches a plateau at 90% above $E > 50$ GeV.

A test-beam measurement, carried out at the Meson Test Beam Facility¹ at the Fermi National Accelerator Laboratory, confirmed the calorimeter's linear energy response and measured the electromagnetic shower shapes. These shower shapes were then used to tune a GEANT 3.21 [37] based full detector simulation. The absolute energy

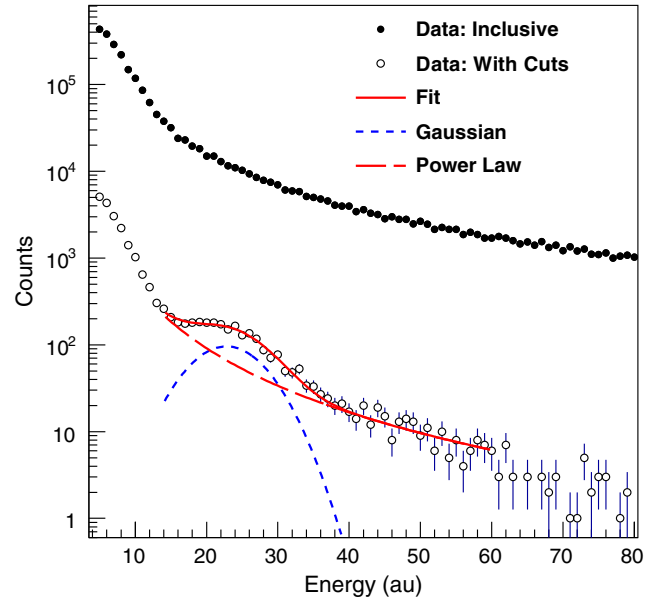


FIG. 1 (color online). Uncalibrated energy spectra with and without cuts to isolate minimum ionizing particles (MIP) in the MPC. These cuts include neighboring tower energy deposits and track-matching cuts using the upstream BBC Čerenkov counters. The spectrum with the cut is fit with a power law and a Gaussian. The Gaussian peak position is taken as the most probable MIP energy deposit, $E \approx 234$ MeV.

scale of the detector is determined *in situ* using a two-step process. First, minimum ionizing particles are used. Yields of charged tracks in the calorimeter are enhanced by requiring a correlated hit in the BBC that is located in front of the MPC. Additionally, the tower multiplicity of the cluster is required to be small compared to a typical electromagnetic shower to increase the hadronic contributions. A sample minimum ionizing particle peak is shown in Fig. 1 with an expected mean energy of 234 MeV. The initial MIP calibration is then used as the seed in an iterative and converging procedure for individual towers that is based on the π^0 peak in the invariant mass distribution. Time dependencies in the tower gains are tracked and corrected for by a monitoring system of LEDs, whose intensities are monitored by PIN diodes. Finally, the overall calibration is verified and the energy resolution is determined by comparing the masses of the π^0 and η peaks in the two-cluster invariant mass distributions between data and a Monte Carlo simulation. A set of representative two-cluster invariant mass peaks is shown in Fig. 2. The relative energy resolution ($\delta E/E$) of the calorimeter is found to be $13\%/\sqrt{E} \oplus 8\%$ with an overall energy scale uncertainty of 2%.

C. Polarized proton beams

RHIC accelerates and stores polarized proton beams at energies up to 255 GeV in two independent rings. The beams collide at several interaction points along the ring.

¹It is now the MT6 area at the Fermilab Test Beam Facility.

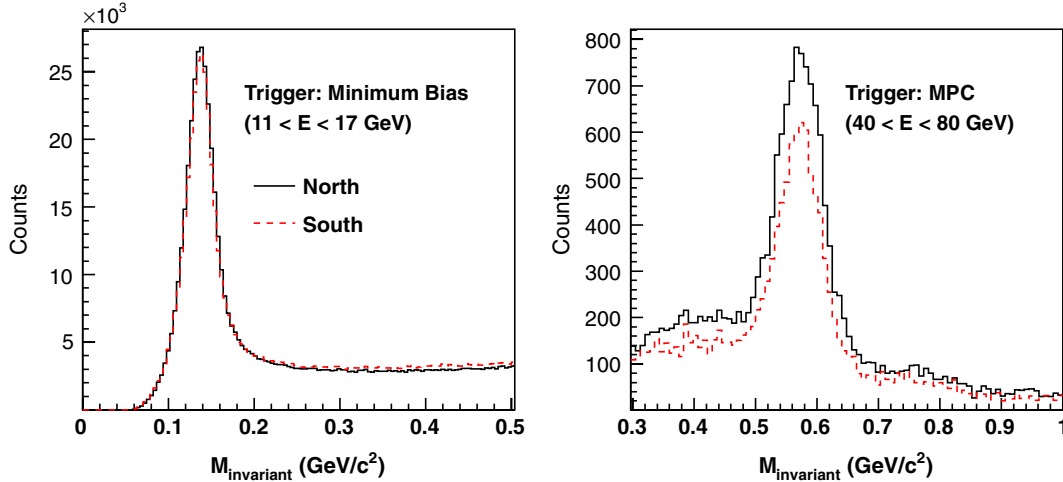


FIG. 2 (color online). Two-cluster invariant mass distributions from the 2008 data set at $\sqrt{s} = 200$ GeV for both the north and south MPC detectors. The left panel shows the π^0 peak from the minimum bias triggered data set at low energy while the right side shows the η meson peak from the MPC triggered data set at high two-cluster energies E . A comparison of the peak position and widths from data and simulation are used to determine the energy scale uncertainty.

Each ring can be filled with up to 120 bunches with different transverse polarization directions. These directions alternate to reduce systematic effects from slow variations in luminosity or detector acceptances and efficiencies. Additionally, the patterns are chosen from four predefined basic patterns to reduce time dependent correlations and detector effects.

Previous publications describe in detail the necessary accelerator instrumentation for producing the colliding polarized beams [38]. The polarization is measured with a set of polarimeters external to the PHENIX experiment using elastic scattering from a hydrogen gas jet or a carbon fiber target. For the determination of the absolute polarization of both proton beams, the hydrogen jet polarimeter with a known polarization of the atomic jet is used [39]. Due to the low density of the gas jet a polarization measurement with good accuracy requires many hours of data taking. Therefore, the relative polarization is measured several times per fill with high precision by fast $p + C$ polarimeters for each of the two storage rings [40]. These relative measurements are then normalized using results from the jet polarimeter.

TABLE I. Polarizations for RHIC proton beams in 2006 and 2008. The polarization uncertainty is a global scale uncertainty of the measured asymmetries A_N and is not included in any of the figures or data tables.

| Year | \sqrt{s} (GeV) | Beam direction | P_{beam} |
|------|------------------|---------------------------------|--------------------|
| 2006 | 62.4 | North, $\vec{p} = (0, 0, p_z)$ | $(49.0 \pm 4.4)\%$ |
| 2006 | 62.4 | South, $\vec{p} = (0, 0, -p_z)$ | $(49.0 \pm 4.4)\%$ |
| 2008 | 200 | North, $\vec{p} = (0, 0, p_z)$ | $(48.0 \pm 4.0)\%$ |
| 2008 | 200 | South, $\vec{p} = (0, 0, -p_z)$ | $(41.0 \pm 4.0)\%$ |

While both of the RHIC beams are polarized during the measurement of the single-spin asymmetries presented in this paper, summation over the bunches of one beam effectively averages the polarization to zero. This procedure is applied to one of the two beams at a time and can therefore be used as a cross-check of two uncorrelated measurements of the asymmetry. The direction of the polarized beam is commonly referred to as forward in the following; backward is in the direction of the unpolarized beam. Table I summarizes the beam polarizations for the different data sets and center-of-mass energies, with $\vec{p} = (0, 0, p_z)$ pointing north, according to the PHENIX coordinate system.

The stable polarization direction around the accelerator is vertical [$P^\uparrow = (0, P, 0)$ or $P^\downarrow = (0, -P, 0)$] and can be changed by spin rotators around the collision points. The transverse components of the polarization vector are measured locally in PHENIX. In 2008, the polarization of the north pointing beam was tilted from the vertical direction by $\varphi_0 = 0.263 \pm 0.030^{\text{stat}} \pm 0.090^{\text{syst}}$ rad. For the rest of the measurements, all other polarization vectors are found to be consistent with the vertical direction within statistical uncertainties [41]. The polarization directions are accounted for in the determination of the relevant asymmetries. In addition, the 2006 and 2008 polarization direction measurements have been independently verified using the analysis techniques from Sec. III A.

III. ANALYSIS

A. Transverse-single-spin asymmetries

The A_N that can generally arise in polarized scattering experiments are described in the framework of polarization analyzing tensors which gives information about fully

polarized initial and final states of the scattering process. The polarization can be aligned along three dimensions in the scattering frame, i.e., longitudinal in the projectile direction \vec{L} , sideways in the scattering (or production) plane \vec{S} , or normal to the scattering plane \vec{N} , where $\vec{S} = \vec{N} \times \vec{L}$. In the following, the left side refers to the direction of \vec{S} in this right-handed system, the right side to the opposite direction. For A_N , we are only considering a normal polarization for the projectile. Target and final states are unpolarized. The normal space quantization can create a transverse asymmetry within the scattering plane. A rotation into the laboratory frame (where the beam polarization P is prepared) then transforms this pure left-right asymmetry into an azimuthal (φ) modulation of the cross section $d\sigma(\varphi) \propto A_N \cdot P \cdot \cos \varphi$. The transverse asymmetry A_N can be determined from pointlike detectors as

$$A_N = \frac{1}{P} \cdot \frac{1}{\cos \varphi} \frac{d\sigma(\varphi) - d\sigma(\varphi + \pi)}{d\sigma(\varphi) + d\sigma(\varphi + \pi)}. \quad (1)$$

The same result can be achieved with a detector in just one hemisphere by a rotation of the polarization vector $P^\uparrow \rightarrow P^\downarrow$:

$$\begin{aligned} d\sigma^\uparrow(\varphi) &= d\sigma^\downarrow(\varphi + \pi) \\ d\sigma^\downarrow(\varphi) &= d\sigma^\uparrow(\varphi + \pi). \end{aligned}$$

Integrating the cross sections over the detector acceptance, beam luminosities, and the duration of the measurement, A_N is experimentally extracted from the geometric means of the particle yields:

$$\epsilon(\varphi) = A_N \cdot P \cdot \cos \varphi = \frac{\sqrt{N_L^\uparrow \cdot N_R^\downarrow} - \sqrt{N_L^\downarrow \cdot N_R^\uparrow}}{\sqrt{N_L^\uparrow \cdot N_R^\downarrow} + \sqrt{N_L^\downarrow \cdot N_R^\uparrow}}, \quad (2)$$

where N_L, N_R refer to particle yields in detector segments $\Delta\varphi$ of the left (φ) and right ($\varphi + \pi$) hemispheres. An alternate estimator is used to study systematic effects:

$$\epsilon(\varphi) = A_N \cdot P \cdot \cos \varphi = \frac{N^\uparrow - \mathcal{R} \cdot N^\downarrow}{N^\uparrow + \mathcal{R} \cdot N^\downarrow}, \quad (3)$$

with \mathcal{R} being the ratio of luminosities between the two spin states \uparrow and \downarrow . This luminosity is determined using the polarization-sorted counts from the minimum bias trigger. The asymmetries in this analysis are calculated in 8 or 16 bins in the azimuth, unless noted otherwise, and then fit to the cosine modulation (with and without an additional free phase φ_0 for consistency checks). Systematic uncertainties are estimated by comparing asymmetries from Eqs. (2) and (3), which may be due to different assumptions in the integration of the cross sections.

B. $A_N^{\pi^0}$ at $\sqrt{s} = 62.4$ GeV and high x_F

Measurements at $\sqrt{s} = 62.4$ GeV were carried out in 2006 with the south MPC, from a total of 3.6×10^7 MPC triggered events. The $\pi^0 \rightarrow \gamma + \gamma$ decay is reconstructed from pairs of clusters in the detector with a selection on the photon shower shape. Clusters which have their central tower marked as either noisy or inactive are removed from the analysis. The π^0 contribution is selected from the cluster pairs by requiring a minimum pair energy, $E_{\text{pair}} > 6$ GeV, and an upper limit of 0.6 on the energy asymmetry α of the two cluster energies E_1 and E_2 ,

$$\alpha = \left| \frac{E_1 - E_2}{E_1 + E_2} \right|. \quad (4)$$

The two cluster invariant mass distributions look qualitatively similar to those from $\sqrt{s} = 200$ GeV shown in Fig. 2. The shape of the distributions has been studied in simulations based on the PYTHIA event generator [42] Tune A [43] with a full detector simulation (similar to Sec. II B). The background is dominated by combinatorial effects from reconstructing two clusters from different parent sources. The background yield is determined by mixing uncorrelated clusters from different events and normalizing to the invariant mass distribution above the π^0 peak, but below any contribution from the η peak. From the integral of the resulting π^0 peak one can determine the π^0 yields. The final asymmetries are calculated according to Eq. (2) from the geometrical means of the π^0 yields. The systematic uncertainties to these asymmetries are estimated using Eq. (3).

Figure 3 shows A_N at $\sqrt{s} = 62.4$ GeV as a function of $x_F = 2 \cdot p_z / \sqrt{s}$, with p_z being the longitudinal component

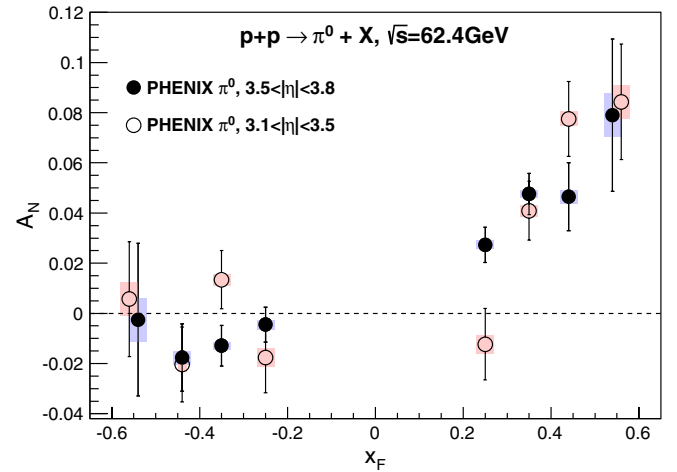


FIG. 3 (color online). Neutral pion A_N at $\sqrt{s} = 62.4$ GeV as a function of x_F in two different pseudorapidity ranges ($3.1 < |\eta| < 3.5$ and $3.5 < |\eta| < 3.8$) with statistical and systematic uncertainties. Appendix Table III gives the data in plain text. An additional uncertainty from the beam polarization (see Table I) is not included.

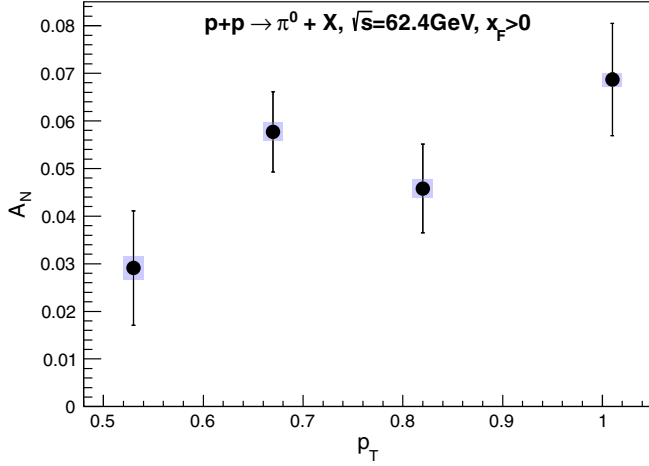


FIG. 4 (color online). Neutral pion A_N at $\sqrt{s} = 62.4$ GeV as a function of transverse momentum p_T . Appendix Table IV gives the plain text data. An additional uncertainty from the beam polarization (see Table I) is not included.

of the momentum along the direction of the polarized proton beam. While there is a significant, nonzero asymmetry rising with $x_F > 0$ in the forward direction, no such behavior can be seen at negative $x_F < 0$ where the asymmetries are consistent with zero. Figure 4 shows the p_T dependence of A_N for all $x_F > 0$. The p_T is largely limited by kinematics due to the low 62.4 GeV center-of-mass energy. No strong p_T dependence is observed for the wide range of x_F that has been included.

Figure 5 compares the x_F dependence of neutral pion A_N of this publication with the world data set [10,11] at center-of-mass energies from $\sqrt{s} = 19.4$ to 200 GeV. Although the different measurements were carried out with slightly different detector acceptances, there is a general agreement between the asymmetries in the onset of nonvanishing

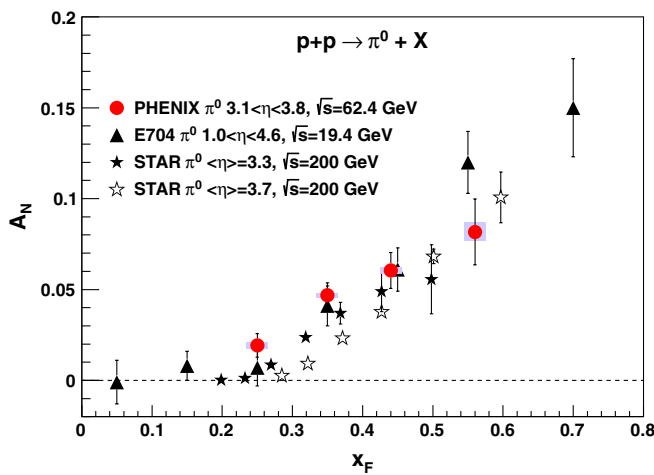


FIG. 5 (color online). Comparison of neutral pion A_N as a function of x_F from $\sqrt{s} = 19.4$ to 200 GeV from this publication and [7,11]. Appendix Table V gives the data in plain text.

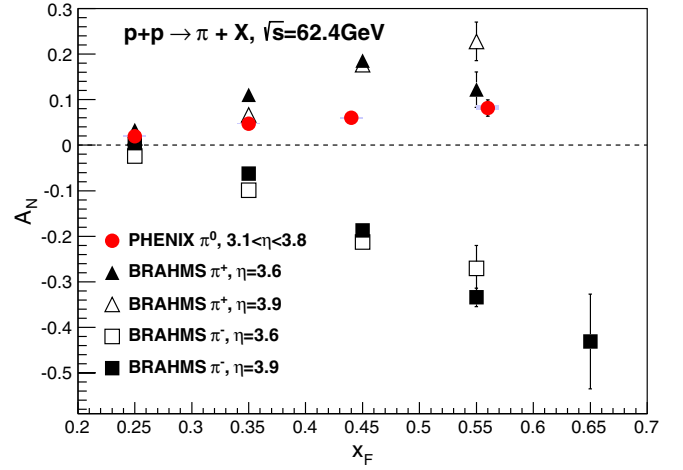


FIG. 6 (color online). Isospin comparison of pion A_N as a function of x_F at $\sqrt{s} = 62.4$ GeV from this publication and [10]. Appendix Table V gives the data in plain text.

asymmetries and the x_F dependence. The asymmetries appear to be independent of the center-of-mass energy, including at high energies where the applicability of pQCD is well established at $\sqrt{s} = 200$ GeV at $p_T > 2$ GeV/c.

Figure 6 shows the pion isospin dependence of A_N at $\sqrt{s} = 62.4$ GeV with combined RHIC data from the new π^0 PHENIX data and charged pion data from the BRAHMS Collaboration [10]. The BRAHMS measurements of charged pions were carried out with two detector settings covering different subranges in pseudorapidity which compare well to the acceptance of the MPC. While π^+ and π^0 asymmetries are positive, those of π^- are of opposite sign. The amplitudes of the charged pion asymmetries are of similar size, with the π^- perhaps slightly larger, whereas both are significantly larger than the neutral pion asymmetry.

C. A_N^{cluster} at $\sqrt{s} = 200$ GeV and high x_F

At energies below $E_{\pi^0} \lesssim 20$ GeV the MPC is able to resolve the $\pi^0 \rightarrow \gamma + \gamma$ decay. However, with increasing energy, the opening angle between the two photons becomes so small that their electromagnetic clusters fully merge in the detector. This limits the x_F range at $\sqrt{s} = 200$ GeV to below 0.2 for π^0 's reconstructed via the two-photon decay mode. To overcome this limitation the data analysis is done for inclusive clusters.

The data set at $\sqrt{s} = 200$ GeV includes 1.8×10^8 events recorded with a high energy cluster trigger. Clusters in the analysis are required to have fired the corresponding trigger, i.e., N-MPC or S-MPC, and to satisfy a time of flight cut. Clusters whose central tower is marked as either noisy or inactive are removed from the analysis. The contributions from hadrons to the cluster yields are reduced by selecting for photonic shower shapes. To minimize effects from energy leakage at the detector edges, a radial

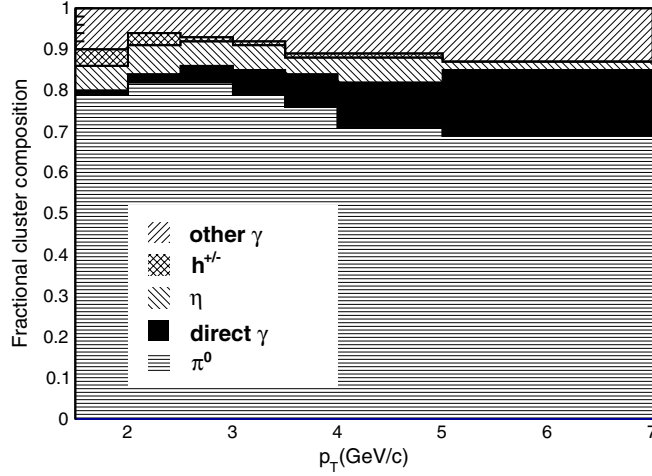


FIG. 7 (color online). Cluster composition from $p + p$ Monte Carlo event generator studies at $\sqrt{s} = 200$ GeV with a full detector simulation. The kinematic cuts and p_T ranges are the same as those used in the data analysis and directly comparable to Fig. 9, in particular $x_F > 0.4$.

fiducial cut is applied. The transverse asymmetries are determined with Eq. (2) and systematic uncertainties are estimated using the difference from Eq. (3).

The cluster composition is estimated using Monte Carlo simulations to give a qualitative understanding of the relative contributions to the measured clusters. Again, a full detector simulation is based on input from PYTHIA 6.421 Tune A with separate normalization factors between direct photons ($k = 2$) and all other particles originating from high energy scattering processes ($k = 1$) with a minimum p_T of 2 GeV. The normalization factors are determined by comparing the simulated cross sections with RHIC measurements at $\sqrt{s} = 200$ GeV [44–47]. The composition analysis differentiates between electromagnetic clusters originating from photonic decays of π^0 and η mesons, direct photons, and energy deposited by charged hadrons (h^\pm). Contributions from other sources, e.g. fragmentation photons and ω meson decays, are combined in the “other γ ” category.

Figure 7 summarizes the cluster composition as a function of p_T with large $x_F > 0.4$; Table II lists the

TABLE II. Fractional composition of electromagnetic clusters in the MPC at $\sqrt{s} = 200$ GeV for $x_F > 0.4$, as shown in Fig. 7.

| $\langle x_F \rangle$ | $\langle p_T \rangle$ | π^0 | η | direct γ | $h^{+,-}$ | Other γ |
|-----------------------|-----------------------|---------|--------|-----------------|-----------|----------------|
| 0.41 | 1.95 | 0.79 | 0.06 | 0.01 | 0.04 | 0.10 |
| 0.43 | 2.32 | 0.82 | 0.07 | 0.02 | 0.03 | 0.06 |
| 0.45 | 2.77 | 0.82 | 0.06 | 0.04 | 0.01 | 0.06 |
| 0.46 | 3.24 | 0.79 | 0.06 | 0.06 | 0.01 | 0.08 |
| 0.48 | 3.73 | 0.76 | 0.04 | 0.08 | 0.01 | 0.10 |
| 0.49 | 4.40 | 0.71 | 0.06 | 0.11 | 0.01 | 0.11 |
| 0.55 | 5.51 | 0.69 | 0.02 | 0.16 | 0.00 | 0.13 |

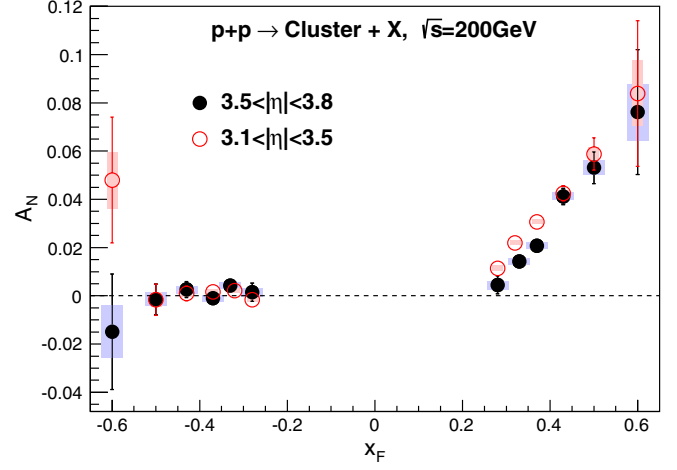


FIG. 8 (color online). The A_N of electromagnetic clusters at $\sqrt{s} = 200$ GeV as a function of x_F and in two different pseudorapidity ranges. Appendix Table VI gives the data in plain text. An additional uncertainty from the beam polarization (see Table I) is not included.

corresponding values in detail. In the context of this PYTHIA study, over the studied kinematic range contributions from decay photons of π^0 mesons are the dominant source of clusters in the MPC. With increasing p_T there is a sizable increase in contributions from direct and other photons. The relative uncertainty of the composition from this study at $p_T > 5$ GeV/c is less than 20% and significantly smaller at lower p_T .

Figure 8 summarizes the x_F dependence of the cluster A_N for two different pseudorapidity ranges similar to Fig. 3. Systematic uncertainties again are evaluated by comparison of results from Eqs. (2) and (3). Within statistical

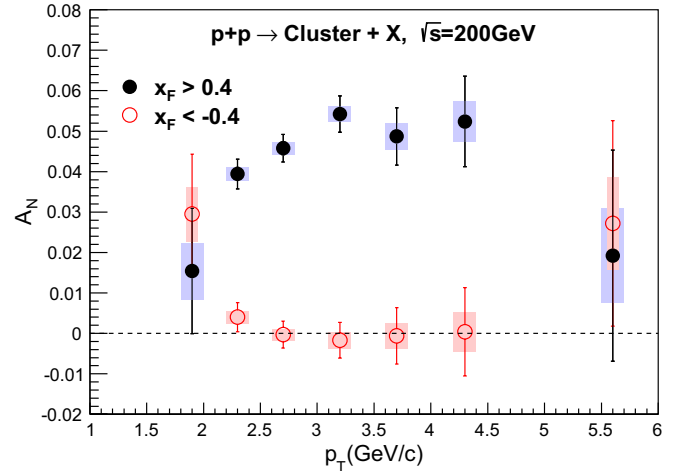


FIG. 9 (color online). The A_N of electromagnetic clusters at $\sqrt{s} = 200$ GeV at large $|x_F| > 0.4$ in forward/backward directions as a function of p_T . Appendix Table VII gives the data in plain text. An additional uncertainty from the beam polarization (see Table I) is not included.

uncertainties the asymmetries in the backward direction $x_F < 0$ are found to be consistent with zero, whereas in the forward direction A_N rises almost linearly with x_F . The asymmetries are of similar size compared to earlier results at different center-of-mass energies as shown in Fig. 5.

Figure 9 presents A_N , as a function of transverse momentum p_T for values of $|x_F| > 0.4$ where A_N is largest in forward kinematics (compare Fig. 8). The asymmetry rises smoothly and then seems to saturate above $p_T > 3$ GeV/ c . A significant decrease of the asymmetry as expected from higher twist calculations is not observed [23]. Again, negative x_F asymmetries are found to be consistent with zero within statistical uncertainties.

Figure 10 shows A_N as a function of p_T for different ranges of x_F . These ranges are chosen to match that of an earlier measurement of π^0 asymmetries from the STAR experiment [11]. The two measurements in general display a good agreement. At large x_F and high p_T there is perhaps a hint that the inclusive cluster asymmetries are smaller, but with present statistics the difference is not yet significant. We note that the STAR measurement is for identified π^0 and the PHENIX measurement is for clusters with a mixed composition. As mentioned previously, these clusters are dominantly from π^0 's, but also include contributions from

the decays of η and other neutral mesons, as well as a contribution from direct photons which is increasing with x_F and p_T .

D. $A_N^{\pi^0, \eta}$ at $\sqrt{s} = 200$ GeV and small x_F

The data selection and asymmetry analysis in the midrapidity spectrometer closely follows the procedure of previous analyses [17]. The data set includes 6.9×10^8 events triggered by the high p_T photon trigger. Photon clusters are selected using photonic shower shape cuts in the electromagnetic calorimeter, the time of flight between the collision point and the calorimeter, a minimum deposited energy of 200 MeV, and a charged particle veto from tracking in front of the calorimeter. Cluster pairs are then chosen with an energy asymmetry [Eq. (4)] of less than 0.8 (0.7) for π^0 (η) identification, and by requiring that the photon with the higher energy fired the trigger.

The yields are taken as the number of cluster pairs in a ± 25 MeV/ c^2 window around the mean of the π^0 peak in the invariant mass distribution (± 70 MeV/ c^2 around the mean of the η mass). The width of the π^0 peak decreases from 12 to 9 MeV/ c^2 as p_T increases from 1 to 12 GeV/ c (35 to 25 MeV/ c^2 for the η). The background fractions in the signal windows depend on p_T and range from 29% to

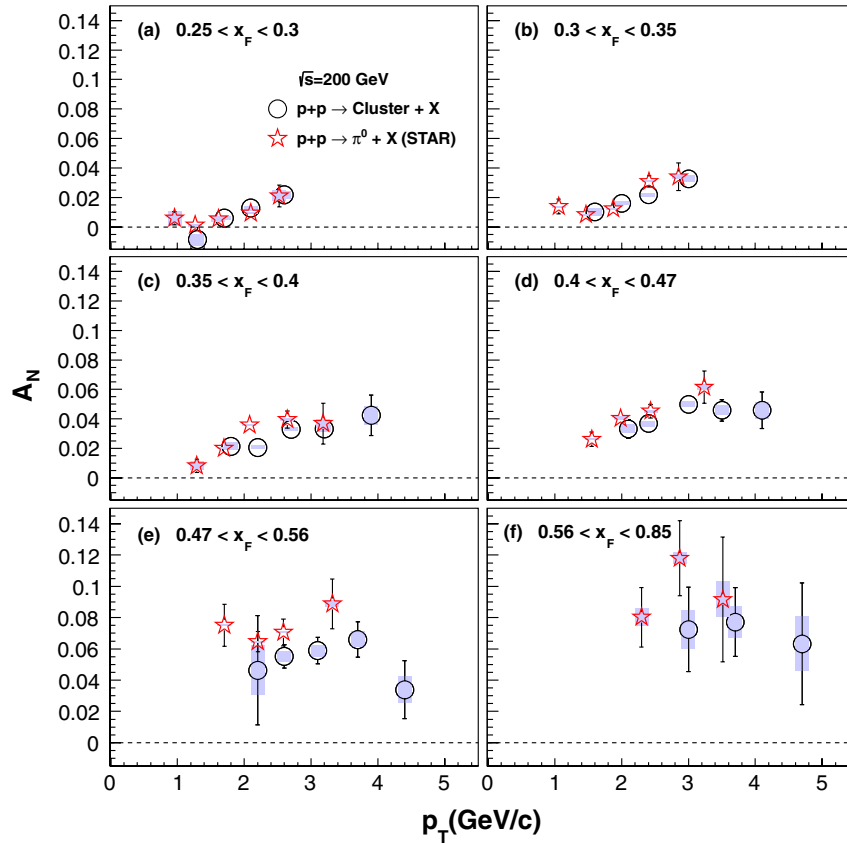


FIG. 10 (color online). Comparison of A_N of electromagnetic clusters and π^0 mesons [11] at $\sqrt{s} = 200$ GeV as a function of p_T in different ranges of x_F . Appendix Table VIII gives the data in plain text. An additional uncertainty from the beam polarization (see Table I) is not included.

4% under the π^0 peak and 75% to 41% for the η peak as p_T increases.

To remove a possible background asymmetry, the weighted asymmetry between a low and high mass region around the signal peak is determined and subtracted from the signal region. These regions are defined from 47 to 97 and from 177 to 227 MeV/ c^2 for the π^0 , and from 300 to 400 and from 700 to 800 MeV/ c^2 for the η meson. As a check, the limits of the background mass regions were varied and no change in the final result was seen. The signal asymmetry A_N^{signal} can be calculated using yields from the peak region N_{incl} and from the interpolated background yields N_{bg} :

$$A_N^{\text{signal}} = \frac{A_N^{\text{incl}} - rA_N^{\text{bg}}}{1 - r}, \quad (5)$$

with the background fraction $r = N_{\text{bg}}/N_{\text{incl}}$ under either the π^0 or η signal. The background asymmetries are all consistent with zero.

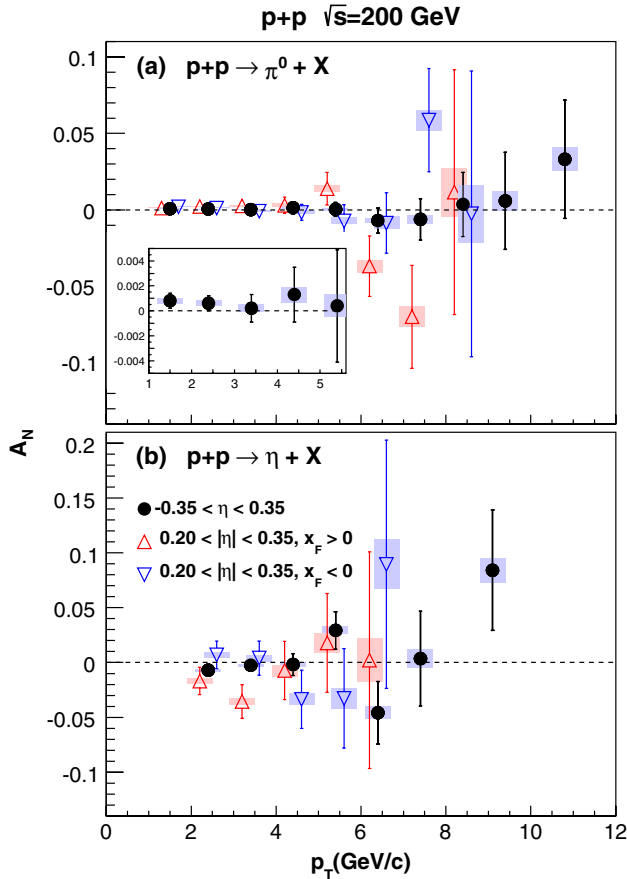


FIG. 11 (color online). The A_N measured at midrapidity ($|\eta| < 0.35$), as a function of p_T for π^0 (a) and η (b) mesons (see Tables IX and X). Triangles are slightly forward/backward going subsamples of the full data set (circles). These are shifted in p_T for better visibility. An additional uncertainty from the beam polarization (see Table I) is not included.

Due to the limited azimuthal acceptance of the mid-rapidity spectrometer the asymmetries are only measured from integrated yields in the whole detector hemispheres to the left and right of the polarization direction. To account for the cosine modulation of the particle production, the asymmetries need to be corrected by an average factor $f = 1/\langle \cos \varphi \rangle$ taken over the detector acceptance. The asymmetries are calculated from Eq. (2), and the corresponding systematic uncertainties are estimated from differences with Eq. (3).

Both the inclusive and background asymmetries are determined for each RHIC fill to test for possible variations with time. The mean values are then used for the calculation of the final asymmetries for π^0 and η mesons as a function of p_T ; see Fig. 11 and Tables IX and X. The figure shows the asymmetries for the whole detector acceptance ($|\eta| < 0.35$) and for two samples selecting slightly forward/backward going particles ($0.2 < |\eta| < 0.35$). It is important to note that the data in the restrictive pseudorapidity ranges are subsamples of the larger inclusive data set. These very precise results are all consistent with zero over the observed p_T range.

IV. DISCUSSION

The A_N of neutral pions and inclusive charged hadrons have previously been measured with the PHENIX mid-rapidity spectrometer [17]. Those asymmetries have been found to be consistent with zero and have been used to constrain the gluon Sivers function [18] despite their limited statistical precision. The new results shown in Fig. 11 exceed the former precision by a factor of 20 for the π^0 transverse asymmetries while extending the p_T reach to above 10 GeV/ c . Also, this paper reports on A_N of η mesons at $x_F \approx 0$ which extends previous results [48] both in \sqrt{s} and p_T . Altogether, no significant deviation from zero can be seen in the results within the statistical uncertainties in the covered transverse momentum range. Any difference in the two meson asymmetries would likely be dominated by fragmentation effects. Either these are small or suppressed by the contributing transversity distribution in the covered kinematic range.

In the forward direction, nonvanishing meson asymmetries persist all the way up to $\sqrt{s} = 200$ GeV, as shown in Figs. 3 and 8. While there is no asymmetry in the backward direction ($x_F < 0$), A_N scales almost linearly with positive $x_F > 0.2$. This behavior is similar to previous experimental results, as summarized in Fig. 5, where no strong center-of-mass energy dependence of the asymmetry is observed. The kinematic coverage of the experiments is not exactly the same and may account for the small differences in the data, but it is striking how well the data match between measurements taken over center-of-mass collision energies that vary by more than an order of magnitude, from $\sqrt{s} = 19.4$ to 200 GeV. If the same mechanisms are responsible across this entire collision energy range, then these

mechanisms seem to have a weak dependence over the interaction scale Q spanned by the world's data.

At forward rapidity x_F is linearly proportional to the polarized parton momentum fraction x_1 :

$$x_F \equiv 2p_L/\sqrt{s} \approx 2\langle z \rangle p_{\text{jet}}/\sqrt{s} \approx \langle z \rangle x_1, \quad (6)$$

where $\langle z \rangle$ is the mean momentum fraction of the hadron from the jet fragmentation. This suggests the possibility that these asymmetries are largely created by some intrinsic function of x that is only weakly dependent on the collision energy.

Further, from a comparison of the asymmetries of the pion isospin triplet at $\sqrt{s} = 62.4$ GeV (see Fig. 6), one can conclude that the Sivvers effect is not the dominant source of the observed transverse asymmetries. PYTHIA event generator studies show that the production of π^- is almost equally from unfavored u and favored d quark fragmentation, while π^+ production is almost exclusively from favored u quark fragmentation. At the same time, about three in four π^0 stem from u quarks, with the other fourth coming from d quarks. Because the Sivvers effect comes from the initial state quarks, the data cannot be explained by these initial state effects alone, under the assumption that the ratio of the u and d quark Sivvers functions (especially at high x) are the same as those extracted from SIDIS [49]. According to these assumptions, one should naively expect a small Sivvers effect asymmetry for the π^- , which has roughly equivalent and canceling contributions from u and d quarks. Instead a large asymmetry is observed for the π^- .

Collinear higher twist calculations predict that A_N decreases with increasing transverse momentum once p_T is of the same order as the partonic momentum scale Q and both are much larger than Λ_{QCD} [23]. Where this turnover of the initially rising A_N happens is largely unknown, though. The cluster asymmetries in Fig. 9 have an extended p_T range compared to previous measurements of π^0 mesons [11], but the data still do not allow for a conclusive answer for the onset of this drop of the asymmetry up to $p_T > 4$ GeV/ c .

The electromagnetic cluster contributions at $\sqrt{s} = 200$ GeV are dominated by π^0 decays, as demonstrated in Fig. 7. With rising p_T , the fraction of direct and other photons increases while the contribution from η mesons does not change significantly. A comparison of the cluster asymmetries with those of π^0 mesons from STAR [11] in Fig. 10 is largely consistent at small x_F and statistically limited at $x_F > 0.47$, where the direct photon contribution to the inclusive clusters becomes more important. Transverse asymmetries of direct photons are of special interest in the future because they directly relate to the Sivvers effect and its process dependence [50].

The data presented in this paper provide crucial input to the long-standing question of the source of A_N in hadronic collisions. The extended statistics of A_N measurements for

π^0 and η at midrapidity, the cluster A_N at 200 GeV, the complete isospin triplet of asymmetries at 62.4 GeV, and the extended range over beam collision energies all quantitatively test the various theories seeking to explain these asymmetries. In particular, the high statistics midrapidity data strongly constrain the presence of a gluon Sivvers effect at midrapidity. The PHENIX data on π^0 transverse asymmetries, along with the world data, do not allow for a strong evolution with Q^2 in the combined effects from whatever causes these asymmetries. Finally, the mix of favored versus unfavored fragmentation for the three different pion states, and how these contribute to the asymmetries, also place constraints on the strengths of the contributing effects.

ACKNOWLEDGMENTS

We thank the staff of the Collider-Accelerator and Physics Departments at Brookhaven National Laboratory and the staff of the other PHENIX participating institutions for their vital contributions. We acknowledge support from the Office of Nuclear Physics in the Office of Science of the Department of Energy; the National Science Foundation; a sponsored research grant from Renaissance Technologies LLC; Abilene Christian University Research Council; Head of Department of Physics, University of Illinois at Urbana Champaign; Research Foundation of SUNY; and Dean of the College of Arts and Sciences, Vanderbilt University (U.S.A.); Ministry of Education, Culture, Sports, Science, and Technology; the Japan Society for the Promotion of Science; and Head Investigator, Graduate School of Science, Hiroshima University (Japan); Conselho Nacional de Desenvolvimento Científico e Tecnológico and Fundação de Amparo à Pesquisa do Estado de São Paulo (Brazil); Natural Science Foundation of China (P. R. China); Ministry of Education, Youth and Sports (Czech Republic); Centre National de la Recherche Scientifique; Commissariat à l'Énergie Atomique; and Institut National de Physique Nucléaire et de Physique des Particules (France); Bundesministerium für Bildung und Forschung; Deutscher Akademischer Austausch Dienst; and Alexander von Humboldt Stiftung (Germany); Hungarian National Science Fund, OTKA (Hungary); Department of Atomic Energy and Department of Science and Technology (India); Israel Science Foundation (Israel); National Research Foundation and WCU program of the Ministry Education Science and Technology (Korea); Physics Department, Lahore University of Management Sciences (Pakistan); Ministry of Education and Science; Russian Academy of Sciences; Federal Agency of Atomic Energy; and Program Coordinator, Russian Research Center, Kurchatov Institute (Russia); VR and Wallenberg Foundation (Sweden); the U.S. Civilian Research and Development Foundation for the Independent States of the Former Soviet Union; the U.S.-Hungarian Fulbright Foundation for Educational Exchange; and the U.S.-Israel Binational Science Foundation.

APPENDIX

Below are data tables of measured A_N with statistical and systematic uncertainties and cluster composition for cluster asymmetries at forward pseudorapidities.

TABLE III. The A_N at $\sqrt{s} = 62.4$ GeV as a function of x_F for two pseudorapidity ranges, as shown in Fig. 3.

| | $\langle x_F \rangle$ | $\langle p_T \rangle$ | $A_N \pm \sigma_{\text{stat}} \pm \sigma_{\text{syst}}(x_F > 0)$ | $A_N \pm \sigma_{\text{stat}} \pm \sigma_{\text{syst}}(x_F < 0)$ |
|----------------------|-------------------------|-----------------------|--|--|
| $3.1 < \eta < 3.5$ | 0.25 | 0.41 | $-0.0123 \pm 0.0142 \pm 0.0037$ | $-0.0176 \pm 0.0141 \pm 0.0037$ |
| $3.1 < \eta < 3.5$ | 0.35 | 0.59 | $0.0409 \pm 0.0117 \pm 0.0023$ | $0.0134 \pm 0.0116 \pm 0.0023$ |
| $3.1 < \eta < 3.5$ | 0.44 | 0.74 | $0.0775 \pm 0.0149 \pm 0.0029$ | $-0.0204 \pm 0.0149 \pm 0.0029$ |
| $3.1 < \eta < 3.5$ | 0.56 | 0.92 | $0.0843 \pm 0.0230 \pm 0.0066$ | $0.0057 \pm 0.0229 \pm 0.0066$ |
| $3.5 < \eta < 3.8$ | 0.25 | 0.56 | $0.0273 \pm 0.0070 \pm 0.0018$ | $-0.0045 \pm 0.0070 \pm 0.0018$ |
| $3.5 < \eta < 3.8$ | 0.35 | 0.77 | $0.0476 \pm 0.0082 \pm 0.0016$ | $-0.0129 \pm 0.0081 \pm 0.0016$ |
| $3.5 < \eta < 3.8$ | 0.44 | 0.95 | $0.0465 \pm 0.0135 \pm 0.0026$ | $-0.0176 \pm 0.0134 \pm 0.0026$ |
| $3.5 < \eta < 3.8$ | 0.54 | 1.15 | $0.0790 \pm 0.0304 \pm 0.0087$ | $-0.0025 \pm 0.0304 \pm 0.0087$ |

TABLE IV. The A_N as a function of p_T at $\sqrt{s} = 62.4$ GeV, as shown in Fig. 4.

| | $\langle p_T \rangle$ | $\langle x_F \rangle$ | $A_N \pm \sigma_{\text{stat}} \pm \sigma_{\text{syst}}(x_F > 0)$ | $A_N \pm \sigma_{\text{stat}} \pm \sigma_{\text{syst}}(x_F < 0)$ |
|--------------------|-----------------------|-------------------------|--|--|
| $3.1 < \eta < 3.8$ | 0.53 | 0.29 | $0.0291 \pm 0.0120 \pm 0.0025$ | $-0.0091 \pm 0.0117 \pm 0.0025$ |
| $3.1 < \eta < 3.8$ | 0.67 | 0.34 | $0.0577 \pm 0.0084 \pm 0.0019$ | $-0.0055 \pm 0.0081 \pm 0.0018$ |
| $3.1 < \eta < 3.8$ | 0.82 | 0.39 | $0.0458 \pm 0.0093 \pm 0.0019$ | $-0.0227 \pm 0.0093 \pm 0.0019$ |
| $3.1 < \eta < 3.8$ | 1.01 | 0.45 | $0.0687 \pm 0.0118 \pm 0.0014$ | $-0.0112 \pm 0.0114 \pm 0.0013$ |

TABLE V. The A_N at $\sqrt{s} = 62.4$ GeV as a function of x_F , as shown in Figs. 5 and 6.

| | $\langle x_F \rangle$ | $\langle p_T \rangle$ | $A_N \pm \sigma_{\text{stat}} \pm \sigma_{\text{syst}}(x_F > 0)$ | $A_N \pm \sigma_{\text{stat}} \pm \sigma_{\text{syst}}(x_F < 0)$ |
|----------------------|-------------------------|-----------------------|--|--|
| $3.1 < \eta < 3.8$ | 0.25 | 0.52 | $0.0193 \pm 0.0065 \pm 0.0017$ | $-0.0067 \pm 0.0065 \pm 0.0017$ |
| $3.1 < \eta < 3.8$ | 0.35 | 0.71 | $0.0469 \pm 0.0067 \pm 0.0013$ | $-0.0017 \pm 0.0066 \pm 0.0013$ |
| $3.1 < \eta < 3.8$ | 0.44 | 0.86 | $0.0605 \pm 0.0099 \pm 0.0019$ | $-0.0182 \pm 0.0099 \pm 0.0019$ |
| $3.1 < \eta < 3.8$ | 0.56 | 1.01 | $0.0817 \pm 0.0182 \pm 0.0052$ | $-0.0009 \pm 0.0181 \pm 0.0052$ |

TABLE VI. The A_N at $\sqrt{s} = 200$ GeV as a function of p_T at forward/backward rapidities in two different pseudorapidity ranges, as shown in Fig. 8.

| | $\langle x_F \rangle$ | $\langle p_T \rangle$ (GeV/c) | $A_N \pm \sigma_{\text{stat}} \pm \sigma_{\text{syst}}(x_F > 0)$ | $A_N \pm \sigma_{\text{stat}} \pm \sigma_{\text{syst}}(x_F < 0)$ |
|----------------------|-------------------------|-------------------------------|--|--|
| $3.1 < \eta < 3.5$ | 0.28 | 2.1 | $0.0114 \pm 0.0023 \pm 0.0010$ | $-0.0016 \pm 0.0023 \pm 0.0010$ |
| $3.1 < \eta < 3.5$ | 0.32 | 2.4 | $0.0219 \pm 0.0020 \pm 0.0009$ | $0.0022 \pm 0.0020 \pm 0.0009$ |
| $3.1 < \eta < 3.5$ | 0.37 | 2.7 | $0.0307 \pm 0.0022 \pm 0.0010$ | $0.0016 \pm 0.0023 \pm 0.0010$ |
| $3.1 < \eta < 3.5$ | 0.43 | 3.1 | $0.0425 \pm 0.0031 \pm 0.0014$ | $0.0010 \pm 0.0030 \pm 0.0014$ |
| $3.1 < \eta < 3.5$ | 0.50 | 3.6 | $0.0588 \pm 0.0067 \pm 0.0030$ | $-0.0016 \pm 0.0065 \pm 0.0029$ |
| $3.1 < \eta < 3.5$ | 0.60 | 4.3 | $0.0839 \pm 0.0302 \pm 0.0136$ | $0.0480 \pm 0.0261 \pm 0.0117$ |
| $3.5 < \eta < 3.8$ | 0.28 | 1.5 | $0.0045 \pm 0.0037 \pm 0.0017$ | $0.0015 \pm 0.0038 \pm 0.0017$ |
| $3.5 < \eta < 3.8$ | 0.33 | 1.8 | $0.0142 \pm 0.0029 \pm 0.0013$ | $0.0042 \pm 0.0029 \pm 0.0013$ |
| $3.5 < \eta < 3.8$ | 0.37 | 2.0 | $0.0207 \pm 0.0029 \pm 0.0013$ | $-0.0010 \pm 0.0028 \pm 0.0013$ |
| $3.5 < \eta < 3.8$ | 0.43 | 2.3 | $0.0412 \pm 0.0034 \pm 0.0015$ | $0.0026 \pm 0.0033 \pm 0.0015$ |
| $3.5 < \eta < 3.8$ | 0.50 | 2.7 | $0.0531 \pm 0.0066 \pm 0.0030$ | $-0.0015 \pm 0.0064 \pm 0.0029$ |
| $3.5 < \eta < 3.8$ | 0.60 | 3.2 | $0.0762 \pm 0.0259 \pm 0.0117$ | $-0.0149 \pm 0.0239 \pm 0.0108$ |

TABLE VII. The A_N at $\sqrt{s} = 200$ GeV in forward/backward rapidities ($|x_F| > 0.4$), as shown in Fig. 9.

| | $\langle x_F \rangle$ | p_T (GeV/c) | $A_N \pm \sigma_{\text{stat}} \pm \sigma_{\text{syst}}(x_F > 0)$ | $A_N \pm \sigma_{\text{stat}} \pm \sigma_{\text{syst}}(x_F < 0)$ |
|----------------------|-------------------------|---------------|--|--|
| $3.1 < \eta < 3.8$ | 0.41 | 1.9 | $0.0154 \pm 0.0155 \pm 0.0070$ | $0.0295 \pm 0.0148 \pm 0.0067$ |
| $3.1 < \eta < 3.8$ | 0.43 | 2.3 | $0.0394 \pm 0.0037 \pm 0.0017$ | $0.0040 \pm 0.0036 \pm 0.0016$ |
| $3.1 < \eta < 3.8$ | 0.44 | 2.7 | $0.0458 \pm 0.0034 \pm 0.0015$ | $-0.0003 \pm 0.0033 \pm 0.0015$ |
| $3.1 < \eta < 3.8$ | 0.46 | 3.2 | $0.0542 \pm 0.0045 \pm 0.0020$ | $-0.0017 \pm 0.0044 \pm 0.0020$ |
| $3.1 < \eta < 3.8$ | 0.47 | 3.7 | $0.0487 \pm 0.0071 \pm 0.0032$ | $-0.0006 \pm 0.0070 \pm 0.0031$ |
| $3.1 < \eta < 3.8$ | 0.49 | 4.3 | $0.0524 \pm 0.0112 \pm 0.0050$ | $0.0004 \pm 0.0109 \pm 0.0049$ |
| $3.1 < \eta < 3.8$ | 0.62 | 5.6 | $0.0192 \pm 0.0261 \pm 0.0117$ | $0.0272 \pm 0.0254 \pm 0.0114$ |

TABLE VIII. The A_N as a function of p_T and x_F at forward/backward rapidities, as shown in Fig. 10.

| $\langle x_F \rangle$ | $\langle p_T \rangle$ (GeV/c) | $A_N \pm \sigma_{\text{stat}} \pm \sigma_{\text{syst}}(x_F > 0)$ | $A_N \pm \sigma_{\text{stat}} \pm \sigma_{\text{syst}}(x_F < 0)$ |
|-------------------------|-------------------------------|--|--|
| 0.27 | 1.3 | $-0.0085 \pm 0.0088 \pm 0.0039$ | $0.0176 \pm 0.0088 \pm 0.0040$ |
| 0.28 | 1.7 | $0.0061 \pm 0.0029 \pm 0.0013$ | $-0.0011 \pm 0.0030 \pm 0.0013$ |
| 0.28 | 2.1 | $0.0128 \pm 0.0032 \pm 0.0014$ | $-0.0029 \pm 0.0032 \pm 0.0014$ |
| 0.28 | 2.6 | $0.0219 \pm 0.0058 \pm 0.0026$ | $-0.0064 \pm 0.0057 \pm 0.0026$ |
| 0.32 | 1.6 | $0.0101 \pm 0.0053 \pm 0.0024$ | $0.0037 \pm 0.0053 \pm 0.0024$ |
| 0.32 | 2.0 | $0.0161 \pm 0.0024 \pm 0.0011$ | $0.0052 \pm 0.0025 \pm 0.0011$ |
| 0.33 | 2.4 | $0.0219 \pm 0.0028 \pm 0.0013$ | $0.0026 \pm 0.0029 \pm 0.0013$ |
| 0.33 | 3.0 | $0.0326 \pm 0.0045 \pm 0.0020$ | $-0.0042 \pm 0.0045 \pm 0.0020$ |
| 0.37 | 1.8 | $0.0214 \pm 0.0060 \pm 0.0027$ | $0.0032 \pm 0.0058 \pm 0.0026$ |
| 0.37 | 2.2 | $0.0207 \pm 0.0027 \pm 0.0012$ | $-0.0024 \pm 0.0027 \pm 0.0012$ |
| 0.37 | 2.7 | $0.0330 \pm 0.0029 \pm 0.0013$ | $0.0018 \pm 0.0030 \pm 0.0013$ |
| 0.38 | 3.2 | $0.0333 \pm 0.0054 \pm 0.0024$ | $0.0096 \pm 0.0054 \pm 0.0024$ |
| 0.38 | 3.9 | $0.0424 \pm 0.0137 \pm 0.0062$ | $-0.0041 \pm 0.0135 \pm 0.0061$ |
| 0.42 | 2.1 | $0.0333 \pm 0.0063 \pm 0.0029$ | $0.0020 \pm 0.0061 \pm 0.0027$ |
| 0.43 | 2.4 | $0.0368 \pm 0.0036 \pm 0.0016$ | $0.0003 \pm 0.0035 \pm 0.0016$ |
| 0.43 | 3.0 | $0.0499 \pm 0.0041 \pm 0.0018$ | $0.0038 \pm 0.0040 \pm 0.0018$ |
| 0.43 | 3.5 | $0.0458 \pm 0.0073 \pm 0.0033$ | $0.0012 \pm 0.0071 \pm 0.0032$ |
| 0.44 | 4.1 | $0.0459 \pm 0.0125 \pm 0.0056$ | $-0.0057 \pm 0.0122 \pm 0.0055$ |
| 0.48 | 2.2 | $0.0463 \pm 0.0350 \pm 0.0158$ | $0.0723 \pm 0.0338 \pm 0.0152$ |
| 0.50 | 2.6 | $0.0551 \pm 0.0075 \pm 0.0034$ | $-0.0058 \pm 0.0073 \pm 0.0033$ |
| 0.50 | 3.1 | $0.0589 \pm 0.0084 \pm 0.0038$ | $-0.0043 \pm 0.0082 \pm 0.0037$ |
| 0.50 | 3.7 | $0.0660 \pm 0.0113 \pm 0.0051$ | $0.0080 \pm 0.0109 \pm 0.0049$ |
| 0.51 | 4.4 | $0.0339 \pm 0.0186 \pm 0.0084$ | $-0.0023 \pm 0.0176 \pm 0.0079$ |
| 0.58 | 3.0 | $0.0724 \pm 0.0270 \pm 0.0122$ | $-0.0288 \pm 0.0261 \pm 0.0117$ |
| 0.60 | 3.7 | $0.0772 \pm 0.0221 \pm 0.0100$ | $-0.0044 \pm 0.0212 \pm 0.0095$ |
| 0.61 | 4.7 | $0.0632 \pm 0.0389 \pm 0.0175$ | $0.0453 \pm 0.0375 \pm 0.0169$ |

TABLE IX. The A_N of π^0 mesons at $\sqrt{s} = 200$ GeV at midrapidity as a function of p_T , as shown in Fig. 11. The data in slightly forward and backward kinematics ($0.2 < |\eta| < 0.35$) are subsets of the full data set ($|\eta| < 0.35$).

| $\langle p_T \rangle$ (GeV/c) | $A_N \pm \sigma_{\text{stat}} \pm \sigma_{\text{syst}}$ ($ \eta < 0.35$) | $A_N \pm \sigma_{\text{stat}} \pm \sigma_{\text{syst}}$ ($0.2 < \eta < 0.35, x_F > 0$) | $A_N \pm \sigma_{\text{stat}} \pm \sigma_{\text{syst}}$ ($0.2 < \eta < 0.35, x_F < 0$) |
|-------------------------------|--|---|---|
| 1.5 | $0.0008 \pm 0.0006 \pm 0.0002$ | $0.0012 \pm 0.0014 \pm 0.0003$ | $0.0020 \pm 0.0014 \pm 0.0003$ |
| 2.4 | $0.0006 \pm 0.0006 \pm 0.0002$ | $0.0021 \pm 0.0013 \pm 0.0003$ | $0.0012 \pm 0.0013 \pm 0.0003$ |
| 3.4 | $0.0002 \pm 0.0011 \pm 0.0003$ | $0.0025 \pm 0.0025 \pm 0.0005$ | $-0.0009 \pm 0.0025 \pm 0.0005$ |
| 4.4 | $0.0013 \pm 0.0022 \pm 0.0006$ | $0.0030 \pm 0.0053 \pm 0.0011$ | $-0.0016 \pm 0.0053 \pm 0.0011$ |
| 5.4 | $0.0004 \pm 0.0045 \pm 0.0009$ | $0.0139 \pm 0.0106 \pm 0.0021$ | $-0.0072 \pm 0.0106 \pm 0.0021$ |
| 6.4 | $-0.0071 \pm 0.0082 \pm 0.0016$ | $-0.0368 \pm 0.0197 \pm 0.0039$ | $-0.0086 \pm 0.0198 \pm 0.0040$ |
| 7.4 | $-0.0062 \pm 0.0136 \pm 0.0027$ | $-0.0699 \pm 0.0337 \pm 0.0067$ | $0.0587 \pm 0.0337 \pm 0.0067$ |
| 8.4 | $0.0036 \pm 0.0210 \pm 0.0052$ | $0.0116 \pm 0.0801 \pm 0.0160$ | $-0.0026 \pm 0.0935 \pm 0.0187$ |
| 9.4 | $0.0059 \pm 0.0318 \pm 0.0064$ | ... | ... |
| 10.8 | $0.0331 \pm 0.0387 \pm 0.0077$ | ... | ... |

TABLE X. The A_N of η mesons at $\sqrt{s} = 200$ GeV at midrapidity as a function of p_T , as shown in Fig. 11. The data in slightly forward and backward kinematics ($0.2 < |\eta| < 0.35$) are subsets of the full data set ($|\eta| < 0.35$).

| $\langle p_T \rangle$ (GeV/c) | $A_N \pm \sigma_{\text{stat}} \pm \sigma_{\text{syst}}$ ($ \eta < 0.35$) | $A_N \pm \sigma_{\text{stat}} \pm \sigma_{\text{syst}}$ ($0.2 < \eta < 0.35, x_F > 0$) | $A_N \pm \sigma_{\text{stat}} \pm \sigma_{\text{syst}}$ ($0.2 < \eta < 0.35, x_F < 0$) |
|-------------------------------|--|---|---|
| 2.4 | $-0.0069 \pm 0.0049 \pm 0.0010$ | $-0.0169 \pm 0.0125 \pm 0.0025$ | $0.0070 \pm 0.0126 \pm 0.0025$ |
| 3.4 | $-0.0024 \pm 0.0057 \pm 0.0012$ | $-0.0355 \pm 0.0154 \pm 0.0031$ | $0.0040 \pm 0.0155 \pm 0.0031$ |
| 4.4 | $-0.0019 \pm 0.0099 \pm 0.0020$ | $-0.0073 \pm 0.0265 \pm 0.0053$ | $-0.0336 \pm 0.0265 \pm 0.0053$ |
| 5.4 | $0.0292 \pm 0.0171 \pm 0.0034$ | $0.0178 \pm 0.0452 \pm 0.0090$ | $-0.0327 \pm 0.0453 \pm 0.0091$ |
| 6.4 | $-0.0458 \pm 0.0285 \pm 0.0057$ | $0.0021 \pm 0.0987 \pm 0.0197$ | $0.0896 \pm 0.1131 \pm 0.0226$ |
| 7.4 | $0.0035 \pm 0.0431 \pm 0.0086$ | ... | ... |
| 9.1 | $0.0842 \pm 0.0550 \pm 0.0110$ | ... | ... |

- [1] H.-L. Lai, M. Guzzi, J. Huston, Z. Li, P.M. Nadolsky, J. Pumplin, and C.-P. Yuan, *Phys. Rev. D* **82**, 074024 (2010).
- [2] J. C. Ralston and D.E. Soper, *Nucl. Phys.* **B152**, 109 (1979).
- [3] D. de Florian, R. Sassot, M. Stratmann, and W. Vogelsang, *Phys. Rev. D* **80**, 034030 (2009).
- [4] G. L. Kane, J. Pumplin, and W. Repko, *Phys. Rev. Lett.* **41**, 1689 (1978).
- [5] R. Klem, J. Bowers, H. Courant, H. Kagan, M. Marshak, E. Peterson, K. Ruddick, W. Dragoset, and J. Roberts, *Phys. Rev. Lett.* **36**, 929 (1976).
- [6] J. Antille, L. Dick, L. Madansky, D. Perret-Gallix, M. Werlen, A. Donicé, K. Kuroda, and P. Kyberd, *Phys. Lett.* **94B**, 523 (1980).
- [7] D. L. Adams *et al.* (FNAL-E581 and E704 Collaborations), *Phys. Lett. B* **261**, 201 (1991).
- [8] D. L. Adams *et al.* (FNAL-E704 Collaboration), *Phys. Lett. B* **264**, 462 (1991).
- [9] C. E. Allgower *et al.* (E925 Collaboration), *Phys. Rev. D* **65**, 092008 (2002).
- [10] I. Arsene *et al.* (BRAHMS Collaboration), *Phys. Rev. Lett.* **101**, 042001 (2008).
- [11] B. I. Abelev *et al.* (STAR Collaboration), *Phys. Rev. Lett.* **101**, 222001 (2008).
- [12] L. Adamczyk *et al.* (STAR Collaboration), *Phys. Rev. D* **86**, 032006 (2012).
- [13] L. Adamczyk *et al.* (STAR Collaboration), *Phys. Rev. D* **86**, 051101 (2012).
- [14] D. W. Sivers, *Phys. Rev. D* **41**, 83 (1990).
- [15] C. Adolph *et al.*, *Phys. Lett. B* **717**, 383 (2012).
- [16] A. Airapetian *et al.* (HERMES Collaboration), *Phys. Rev. Lett.* **103**, 152002 (2009).
- [17] S. S. Adler *et al.* (PHENIX Collaboration), *Phys. Rev. Lett.* **95**, 202001 (2005).
- [18] M. Anselmino, U. D'Alesio, S. Melis, and F. Murgia, *Phys. Rev. D* **74**, 094011 (2006).
- [19] J. C. Collins, *Phys. Lett. B* **536**, 43 (2002).
- [20] Z.-B. Kang, J.-W. Qiu, W. Vogelsang, and F. Yuan, *Phys. Rev. D* **83**, 094001 (2011).
- [21] A. V. Efremov and O. V. Teryaev, *Phys. Lett.* **150B**, 383 (1985).
- [22] J.-W. Qiu and G. F. Sterman, *Phys. Rev. Lett.* **67**, 2264 (1991).
- [23] X. Ji, J.-W. Qiu, W. Vogelsang, and F. Yuan, *Phys. Rev. Lett.* **97**, 082002 (2006).
- [24] J. C. Collins, *Nucl. Phys.* **B396**, 161 (1993).
- [25] S. Aoki, M. Doui, T. Hatsuda, and Y. Kuramashi, *Phys. Rev. D* **56**, 433 (1997).
- [26] M. Wakamatsu, *Phys. Rev. D* **79**, 014033 (2009).
- [27] K. Abe *et al.* (Belle Collaboration), *Phys. Rev. Lett.* **96**, 232002 (2006).
- [28] R. Seidl *et al.* (Belle Collaboration), *Phys. Rev. D* **78**, 032011 (2008).
- [29] A. Airapetian *et al.* (HERMES Collaboration), *Phys. Lett. B* **693**, 11 (2010).
- [30] C. Adolph *et al.*, *Phys. Lett. B* **717**, 376 (2012).
- [31] M. Anselmino, M. Boglione, U. D'Alesio, A. Kotzinian, F. Murgia, A. Prokudin, and C. Türk, *Phys. Rev. D* **75**, 054032 (2007).
- [32] M. Anselmino, M. Boglione, U. D'Alesio, E. Leader, S. Melis, F. Murgia, and A. Prokudin, *Phys. Rev. D* **86**, 074032 (2012).
- [33] A. Metz and D. Pitonyak, *Phys. Lett. B* **723**, 365 (2013).
- [34] L. Aphecetche *et al.* (PHENIX Collaboration), *Nucl. Instrum. Methods Phys. Res., Sect. A* **499**, 521 (2003).
- [35] K. Adcox *et al.* (PHENIX Collaboration), *Nucl. Instrum. Methods Phys. Res., Sect. A* **499**, 489 (2003).
- [36] M. Allen *et al.* (PHENIX Collaboration), *Nucl. Instrum. Methods Phys. Res., Sect. A* **499**, 549 (2003).
- [37] R. Brun *et al.*, GEANT Detector Description and Simulation Tool, CERN-W5013 (1994).
- [38] I. Alekseev *et al.*, *Nucl. Instrum. Methods Phys. Res., Sect. A* **499**, 392 (2003).
- [39] I. G. Alekseev *et al.*, *Phys. Rev. D* **79**, 094014 (2009).
- [40] I. Nakagawa *et al.*, *AIP Conf. Proc.* **980**, 380 (2008).
- [41] A. Adare *et al.* (PHENIX Collaboration), *Phys. Rev. D* **82**, 112008 (2010).
- [42] T. Sjostrand, S. Mrenna, and P. Skands, *J. High Energy Phys.* **05** (2006) 026.
- [43] P. Z. Skands, *Phys. Rev. D* **82**, 074018 (2010).

- [44] J. Adams *et al.* (STAR Collaboration), *Phys. Rev. Lett.* **97**, 152302 (2006).
- [45] I. Arsene *et al.* (BRAHMS Collaboration), *Phys. Rev. Lett.* **98**, 252001 (2007).
- [46] S. S. Adler *et al.* (PHENIX Collaboration), *Phys. Rev. Lett.* **98**, 012002 (2007).
- [47] A. Adare *et al.* (PHENIX Collaboration), *Phys. Rev. D* **76**, 051106 (2007).
- [48] D. L. Adams *et al.* (FNAL-E704 Collaboration), *Phys. Lett. B* **276**, 531 (1992).
- [49] M. Anselmino, M. Boglione, U. D'Alesio, A. Kotzinian, S. Melis, F. Murgia, A. Prokudin, and C. Turk, *Eur. Phys. J. A* **39**, 89 (2009).
- [50] L. Gamberg, Z.-B. Kang, and A. Prokudin, *Phys. Rev. Lett.* **110**, 232301 (2013).